De Lucia et al., 2018, Thermochronology links denudation of the Great Unconformity surface to the supercontinent cycle and snowball Earth: Geology, https://doi.org/10.1130/G39525.1.

DATA REPOSITORY: ANALYICAL METHODS AND SUPPLEMENTAL MATERIAL

(U-Th)/He and Apatite Fission Track Methods

Apatite and zircon grains were separated from our samples by standard crushing, sieving, and magnetic and density separation procedures. Single-grain aliquots from each sample were selected for (U-Th)/He analysis performed at the University of Arizona. Analytical methods followed those described in Guenthner et al. (2016) and consisted of diode, Nd:YAG, or CO_2 laser heating; cryogenic purification; and quadrupole mass-spectrometry for ^{4}He analysis; and isotope-dilution high-resolution-inductively coupled plasma-mass spectrometry (HR-ICP-MS) for U and Th analysis. In addition, masses of Zr in zircon grains and Ca in apatite grains were measured following the isotope-dilution protocols of Guenthner et al. (2016). With Zr and Ca measurements from each respective mineral, we can calculate U and Th concentrations (as opposed to just masses) by relating the total measured Zr or Ca in a given aliquot to grain mass through the zircon ($ZrSiO_4$) and apatite ($Ca_5(PO_4)_3F$) chemical formula. Alpha ejection corrections followed Ketcham et al. (2011) for apatite and Hourigan et al. (2005) for zircon. Fission-track analyses were conducted at the University of Arizona following methods described in Thomson et al. (2013). Grains were irradiated at the Oregon State University Triga Reactor, Corvallis, USA and IRMM540R and glass was used to monitor neutron fluence; the zeta calibration factor for apatite (Hurford and Green, 1983) was 368.1 ± 14.9.

Thermal history modeling

Forward model methods and results

We tested several thermal history hypotheses with a series of forward models with ZHe ages predicted using the ZRDAAM zircon (U-Th)/He diffusion model (Guenthner et al., 2013). Guenthner et al. (2013) showed that He diffusivity and radiation damage in zircon coevolve throughout a given grain's thermal history, and if a collection of grains with different effective uranium (eU) concentrations are subjected to the same thermal history, then these grains will possess a range of diffusivities and closure temperatures (T_c). More specifically, increasing amounts of damage initially decrease He diffusivity in zircon, but after accumulated damage exceeds a critical threshold, He diffusivity decreases with further damage. From the perspective

of effective closure temperature, T_c in zircon increases initially with progressive damage accumulation to a threshold after which T_c decreases.

ZRDAAM tests were designed to investigate the timing, magnitude, and style (i.e. single-pulse, two stages of cooling, etc.) of exhumation associated with formation of the Great Unconformity. Given the dearth of *t-T* constraints between 1380 and 500 Ma, our overarching approach was to begin with broad thermal history inputs that bracket a large swath of *t-T* space, and then progressively refine our search. In addition, we considered the possible significance of reheating (burial) and cooling (exhumation) associated with the Keweenawan Midcontinent Rift at ~1100 Ma, and Rodinia break-up in two separate events from ~800-700 Ma and 600-500 Ma (Whitmeyer and Karlstrom, 2007). Because the focus of this bracketing is on the Proterozoic thermal history, for these forward model tests, we fixed the Phanerozoic portion of our thermal histories on the basis of our AFT and AHe results, as well as the observed cessation of sedimentary deposition by the end of the Paleozoic. The inputs for the Phanerozoic were therefore 20 °C at 500 Ma, 100 °C at 250 Ma, 40 °C at 220, and 20 °C at the present day. Combined then, our initial fixed inputs for our forward models consisted of: (1) cooling from high (600 °C) to low (20 °C) temperatures between 1470 and 1380 Ma, representing formation and subsequent cooling to surficial (rhyolite) or hypabyssal (granite) temperatures; (2) a *t-T* point at 20 °C and 500 Ma; and (3) reheating throughout the Paleozoic to reflect the observed sedimentary record, followed by cooling in the Mesozoic to match the AFT and AHe data.

We stress that these inputs are only a first-pass attempt at defining plausible thermal histories for our combined ZHe, AFT, and AHe dataset, and a much broader region of *t-T* space was tested with our inverse models (see additional sections here and in the main text). More complexity may also be warranted beyond these relatively simple heating and cooling *t-T* segments, which can also be tested more effectively in our subsequent inverse models.

The first set of *t-T* brackets between 1380 and 500 Ma consisted of two *t-T* paths: 1) reheating to high temperatures (350 °C) by 1100 Ma, followed by holding and rapid cooling to surface temperatures between 550 and 500 Ma, and 2) holding at surface temperatures between 1380 and 500 Ma. For this first pass, reheating until 1100 Ma was chosen as this time period represents the earliest plausible timing for a tectonic event (the Keweenawan Rift), given the geologic history of the region, that may have affected our sample's thermal history. Again, the period of Proterozoic reheating was more thoroughly explored in the inverse modeling. The

reheating temperature used in the first bracket, 350 °C, is sufficiently high to completely anneal radiation damage in zircon according to the Guenthner et al. (2013) parameterizations. We note that these annealing kinetics rely upon a curvilinear fit to the zircon fission track (ZFT) annealing dataset of Yamada et al. (2007), which yields a partial annealing zone between 310 and 223 °C (0.4-0.8 mean length reduction ratio, respectively, 10 Ma isothermal hold time). Although this annealing model is currently the best available option for modeling damage annealing over geologic timescales, we note that more work is needed to improve this aspect of the ZRDAAM and acknowledge that certain aspects of our modeling could require future refining. However, the ZFT model provides strong constraints on the amount of accumulated damage in our particular setting given that little or no damage annealing occurred after the Neoproterozoic, as evidenced by the relatively low amount of sedimentary burial and absence of major Phanerozoic orogenesis in the area.

Results for this first bracketing experiment are shown in figure 2 in the main text. These results illustrate that our dataset is responsive to the Precambrian thermal history of the Ozark Plateau, as the two *t-T* paths yield distinctive age-eU curves. However, neither curve adequately captures the observed age-eU correlation, which suggests that more complexity is required in the *t-T* paths in order to explain our dataset. To explore additional possible *t-T* paths, we tested a series of refined forward models centered around the major tectonic episodes that could have affected our samples' thermal histories. Following reheating starting at 1380 Ma to a maximum temperature at 1100 Ma, we tested cooling to 20 °C between 600 and 500 Ma (later Rodinia/Pannotia break-up), cooling to 20 °C between 800 and 700 Ma (earlier Rodinia break-up), and cooling to 20 °C between 1100 and 1000 Ma (Keweenawan Rift). We also tested scenarios with relatively longer-term, slower cooling to 20 °C from 1100 to 500 Ma. For each cooling time period, we varied the maximum reheating temperature between 1100 Ma and the time of initial cooling (for example, between 1100 and 600 Ma in the later Rodinia break-up scenario). These maximum reheating or holding temperatures ranged from 250 to 100 °C, and we explored this range by changing the temperature in increments of 10 °C. A summary of these various *t-T* scenarios are shown in Figure S2.

This figure contains the model outputs only from the highest and lowest temperature *t-T* paths from each Precambrian cooling scenario in order to show the ability of each group of paths to bracket (or not) the observed data. For example, Figure S2A shows the model output from two

paths that both have cooling from 1100 to 1000 Ma, but one path has reheating to 250 °C by 1100 Ma and the other has reheating to 100 °C by 1100 Ma. This family of curves fails to bracket the observed data and model ages are too old at almost all eU concentrations, which suggests that the majority of Proterozoic cooling experienced by our samples had to post-date 1000 Ma. This observation is further confirmed by Figures S2B and S2C, which include *t*-*T* paths and model outputs for *t*-*T* scenarios that model cooling either from 800 to 700 Ma or from 600 to 500 Ma, respectively. In both subfigures, intermediate reheating is either to 250 °C or 100 °C. The higher temperature path in figure S2B simulates the consistent set of ~740 Ma ages at low eU concentrations, but fails to capture the age pattern at higher eU concentrations. In figure S2C, the higher temperature path does not reproduce any observed ages, but the combined model results from the two *t*-*T* paths bracket much of the observed dataset. Collectively, these model results shown in figures S2B and S2C suggest that the Proterozoic reheating had to be relatively low (less than 250 °C), and was followed by a significant pulse of cooling between ~800 and 500 Ma that overlaps with the timing of either Rodinia or Pannotia break-up (i.e. must post-date Keweenawan rifting). This break-up timing is more thoroughly investigated in our inverse modeling.

We also examined the influence of a possible short-lived, rapid reheating event as a consequence of the initial break-up of the supercontinent, prior to cooling associated with denudation. Here we focus on a reheating event that occurs from 850 to 840 Ma, followed by cooling back to pre-reheating conditions by 820 Ma, as an example of this possible effect (fig. S3). Two models were run with similar time constraints as figure S2B and S2C, but with constant Neoproterozoic cooling between early (fig. S2B) and late (fig. S2C) Rodinia supercontinent breakup for simplicity. The models differ in the temperature they are held during the Proterozoic (S3A: 180 °C, S3B: 140 °C) to test variable Proterozoic holding temperatures. Short-lived reheating *t*-*T* paths consisted of temperature increases in 20 °C increments at 840 Ma, to a maximum of 400 °C. The results displayed in figure S3, however, end at 340 °C as higher temperatures reset the thermochronologic systems fully and were redundant. Results show that slight reheating events have a relatively minor effect on the model paths, indicated by the similarity in the blue (no reheating) and green (80 °C reheating to 260 °C) envelopes in figure S3A. Further reheating to 340 °C (fig. S3A red envelope) flattens out the envelope erasing the plateau-negative correlation-piedmont pattern seen in prior models, as well as our observed

zircon data. These results suggest that a high temperature, short-lived reheating event prior to Neoproterozoic rifting did not occur in our study area.

A limitation of these forward models is that we have restricted our search to single-phase, linear cooling following reheating at 1100 Ma. We used this approach to demonstrate that distinct Precambrian *t-T* paths yield distinct age-eU correlations (i.e., our data are sensitive to the Proterozoic thermal history of the region) and to define the sets of *t-T* constraints that are, *at a minimum*, required to produce viable paths. But more complex paths, possibly with two pulses of Proterozoic cooling for example, may also provide viable *t-T* solutions. In order to test these more complicated scenarios, we used inverse modeling, as described in the next section.

Inverse model methods

We used HeFTy (version 1.9.1; Ketcham et al., 2005) inverse modeling to further explore viable thermal history scenarios for our samples, with the advantage that inverse modeling can test a far greater number of *t-T* paths. However, when used to test a specific set of *t-T* hypotheses, these methods require user-defined constraint boxes that span regions of *t-T* space, which randomly-generated paths are then forced to pass through in a Monte Carlo simulation. The results from our forward models were used to inform the design of these *t-T* constraint boxes. We created five boxes: 1) a box at 600-550 °C and 1470 to 1380 Ma to simulate granite-rhyolite formation (Rohs, 2013; Bickford et al., 2015), 2) 100-20 °C and 1380 to 1350 Ma to simulate cooling to near-surface temperatures following emplacement or extrusion, 3) 350-100 °C and 1100 to 600 Ma to simulate reheating prior to the various tectonic episodes that we tested for to account for the temperatures necessary to reset the zircon system (Daniel et al., 2013; Dehler et al., 2017; Mulder et al., 2017), 4) 50-20 °C and 550-500 Ma corresponding to subsequent cooling prior to deposition of the lowest Cambrian unit (Ojakangas, 1963), and 5) 200-50 °C and 250 to 200 Ma to model reheating (i.e. burial) throughout the Paleozoic (Liu et al., 2003). A final point was placed at 20 °C at the present day to allow for a wide range of possible Mesozoic and Cenozoic cooling paths. Although some of these *t-T* boxes are narrow to conform with geologic observations, we note that box three is quite extensive to again allow for a wide range of possible Neoproterozoic reheating and cooling scenarios.

In addition to these constraint boxes, inverse model inputs require grain specific information: grain size, eU concentration, and He age. A limitation of HeFTy is that the software

accepts only a certain number of individual grain inputs (7 maximum). More importantly, the HeFTy goodness-of-fit statistics assume that all sources of possible age variation (e.g., radiation damage, grain size, U and Th zonation) are known prior to the model output-data comparison. However, some sources of variation for our dataset, in particular U and Th zonation, are not known for all of the individual grains used here, which is typical for most zircon (U-Th)/He studies. We therefore adopted an averaging approach for the grain-specific information in order to construct our zircon He age-eU inverse models. This approach is similar to one used in age-eU inverse modeling in the apatite He system that relies upon average or "synthetic" grains (Ault et al., 2009; Flowers et al., 2011; Murray et al., 2016). To create these synthetic grains, we divided eU space into discrete bins that were spaced in a manner to best reproduce the range of age, size, and eU of the measured grains. HeFTy limited us to five bins so that AFT and AHe inputs could be used in our models as well. We averaged the grain size and He age of all grains that fell within each bin and used the standard deviation on the mean age as the input uncertainty. Grain specific inputs for zircon He were therefore as follows: 741 ± 21 Ma (eU = 165 ppm, grain size = 39 μm), 726 ± 178 Ma (eU = 311 ppm, grain size = 53 μm), 627 ± 120 Ma (eU = 429 ppm, grain size = 52 μm), 321 ± 60 Ma (eU = 810 ppm, grain size = 43 μm), and 183 ± 5 Ma (eU = 1430 ppm, grain size = 40 μm). The highest eU (~1822 ppm) youngest age (~32 Ma) grain was initially included in this averaging approach as its own individual input. However, with this input, HeFTy produced very few viable *t-T* paths (2 out of 100,000). Other authors have noted that, in some cases, the current damage accumulation and annealing models fail to simulate the correct level of damage in the highest eU grains in a given dataset (Johnson et al., 2017). Previous work and our results here shows that some islands of crystalline material remain in what should otherwise be a metamict zircon with near-zero age, either as a result of low temperature annealing or possibly U and Th zonation. More work is needed to further improve the annealing models for radiation damage in zircon.

For both the AHe and AFT inputs, we used the data from sample 14OZ12, which was the only sample where an AHe age, an AFT age, and AFT track length measurements were all available. The Ketcham et al. (2007) AFT annealing model was used with a c-axis projection of 5.0M and Dpar as determined from Table 3 as the kinetic parameter (1.73 μm). The RDAAM of Flowers et al. (2009) was used for our apatite (U-Th)/He modeling. No age-eU correlation was present in sample 14OZ12 and so we averaged the data from this sample to come up with an age

input of 180.5 ± 44.4 Ma (mean age ± standard deviation), an eU input of 17 ppm, and a grain size input of 54 μm. We used the alpha stopping distances and ejection correction of Ketcham et al. (2011). The results from these inverse models are discussed in the main text.

References:

Supplementary Material and Methods Only Refs

Ault, A.K., Flowers, R.M. & Bowring, S.A. Phanerozoic burial and unroofing history of the western Slave craton and Wopmay orogen from apatite (U–Th)/He thermochronometry. *Earth Planet. Sci. Lett*. **284**, 1-11 (2009).

Bickford, M.E., Van Schmus, W.R., Karlstrom, K.E., Mueller, P.A. & Kamenov, G.D. Mesoproterozoic-trans-Laurentian magmatism: A synthesis of continent-wide age distributions, new SIMS U–Pb ages, zircon saturation temperatures, and Hf and Nd isotopic compositions. *Precambrian Research* **265,** 286-312 (2015).

Daniel, C.G., Pfeifer, L.S., Jones III, J.V. & McFarlane, C.M. Detrital zircon evidence for non-Laurentian provenance, Mesoproterozoic (ca. 1490-1450 Ma) deposition and orogenesis in a reconstructed orogenic belt, northern New Mexico, USA: Defining the Picuris orogeny. *GSA Bulletin* **125**, 1423-1441 (2013).

Dehler, C., Gehrels, G., Porter, S., Heizler, M., Karlstrom, K., Cox, G., Crossey, L. & Timmons, M. Synthesis of the 780-740 Ma Chuar, Uinta Mountain, and Pahrump (ChUMP) groups, western USA: Implications for Laurentia-wide cratonic marine basins. *GSA Bulletin* **129**, 607-624 (2017).

Flowers, R.M., Ketcham, R.A., Shuster, D.L. & Farley, K.A. Apatite (U-Th)/He thermochronometry using a radiation damage accumulation and annealing model. *Geochimica et Cosmochimica Acta* **73,** 2347-2365 (2009).

Flowers, R.M. & Kelly, S.A. Interpreting data dispersion and "inverted" dates in apatite (U–Th)/He and fission-track datasets: An example from the US midcontinent. *Geochimica et Cosmochimica Acta* **75**, 5169–5186 (2011).

Guenthner, W.R., Reiners, P.W., & Chowdhury, U. Isotope dilution analyses of Ca and Zr concentrations of apatite and zircon for (U-Th)/He chronometry. *Geochem. Geophys. Geosyst*. **17**, 1623–1640 (2016).

Hurford, A.J. & Green, P.F. The zeta age calibration of fission-track dating. *Isotope Geoscience* **1**, 285-317 (1983).

Johnson, J.E., Flowers, R.M., Baird, G.B. & Mahan, K.H., "Inverted" zircon and apatite (U-Th)/He dates from the Front Range, Colorado: High-damage zircon as a low-temperature (<50 °C) thermochronometer. *Earth Planet. Sci. Lett*. **466,** 80-90 (2017).

Ketcham, R.A., Carter, A.C., Donelick, R.A., Barbarand, J., Hurford, A.J. "Improved" modeling of Fission-track annealing in apatite. *Am. Min.* **92**, 799-810 (2007).

Ketcham, R.A., Gautheron, C. & Tassan-Got, L. Accounting for long alpha-particle stopping distances in (U–Th–Sm)/He geochronology: Refinement of the baseline case. *Geochimica et Cosmochimica Acta* **75,** 7779–7791 (2011).

Liu, J., Hay, R.L., Deino, A. & Kyser, T.K. Age and origin of authigenic K-feldspar in uppermost Precambrian rocks in the North American Midcontinent. *GSA Bulletin* **115**, 422-433 (2003).

Mulder, J.A., Karlstrom, K.E., Fletcher, K., Heizler, M.T., Timmons, J.M., Crossey, L.J., Gehrels, G.E. & Pecha, M. The syn-orogenic sedimentary record of the Grenville Orogeny in southwest Laurentia. *Precambrian Research* **294**, 33-57 (2017).

Murray, K.E., Reiners, P.W. & Thomson, S.N. Rapid Pliocene–Pleistocene erosion of the central Colorado Plateau documented by apatite thermochronology from the Henry Mountains. *Geology* **44**, 483–486 (2016).

Ojakangas, R.W., 1963, Petrology and sedimentation of the Upper Cambrian Lamotte Sandstone in Missouri: Journal of Sedimentary Research, v. 33, p. 860–873.

Rohs, R.C. Timing of Thermal Overprints in the Silvermines Granite and Associated Diabase Intrusions, St. Francois Mountains, Missouri. *The Compass: Earth Science Journal of Sigma Gamma Epsilon* **85 (3)**, (2013).

Thomson, S.N., Reiners, P.W., Hemming, S.R., and Gehrels, G.E., The contribution of glacial erosion to shaping the hidden landscape of East Antarctica. *Nat. Geosci.* **6,** 203–207 (2013).

Yamada, R., Murakami, M. & Tagami, T. Statistical modeling of annealing kinetics of fission tracks in zircon; reassessment of laboratory experiments. *Chem. Geol*. **236**, 75–91 (2007).

Supplementary Figures:

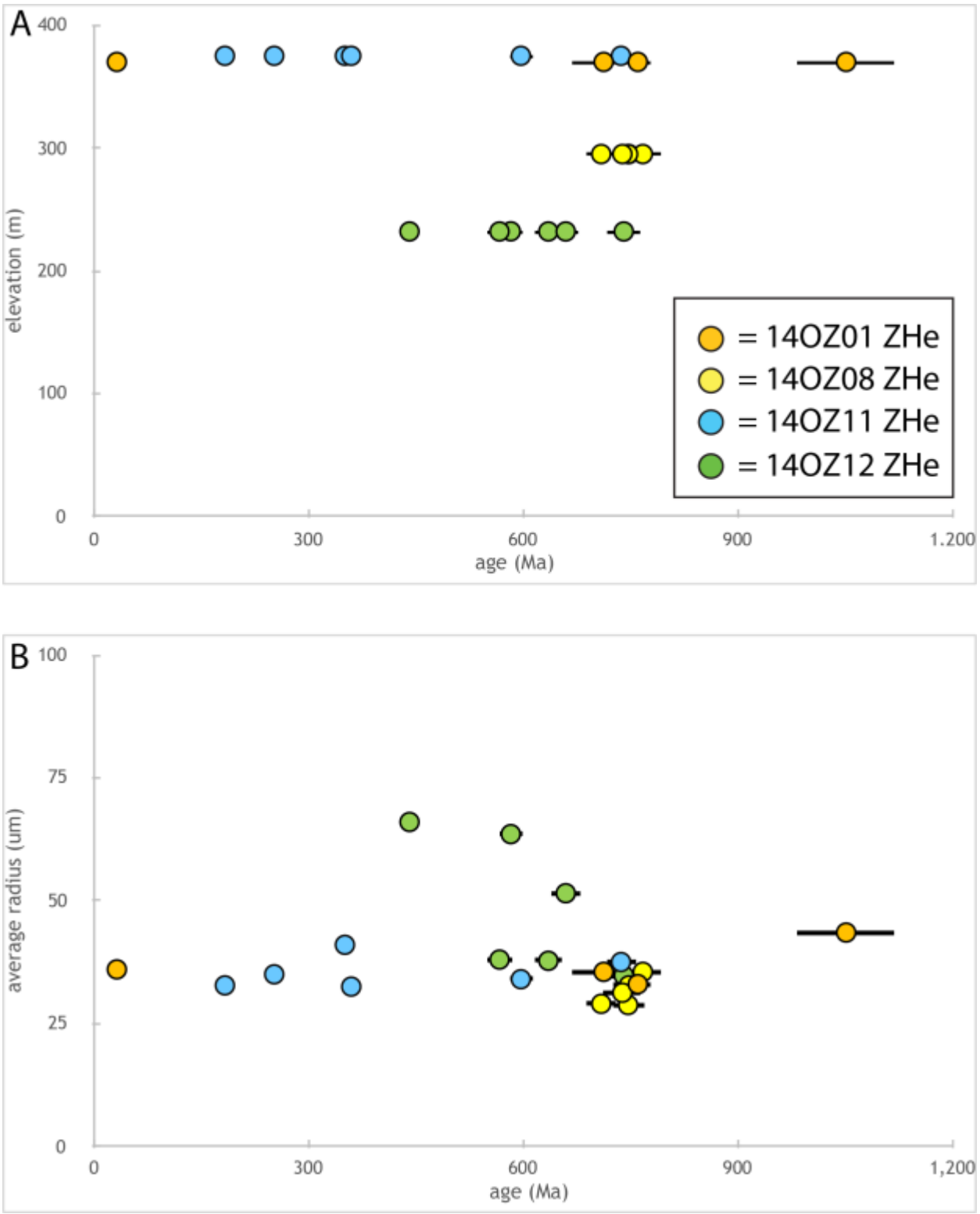

Supplemental Figure DR1: Zircon (U-Th)/He age vs. average radius of the grains (A) and elevation of sample recovery (B). Age error reported as 2 standard deviations. Both plots show no correlation between the age variation of our ZHe data and either grain-size or sample elevation.

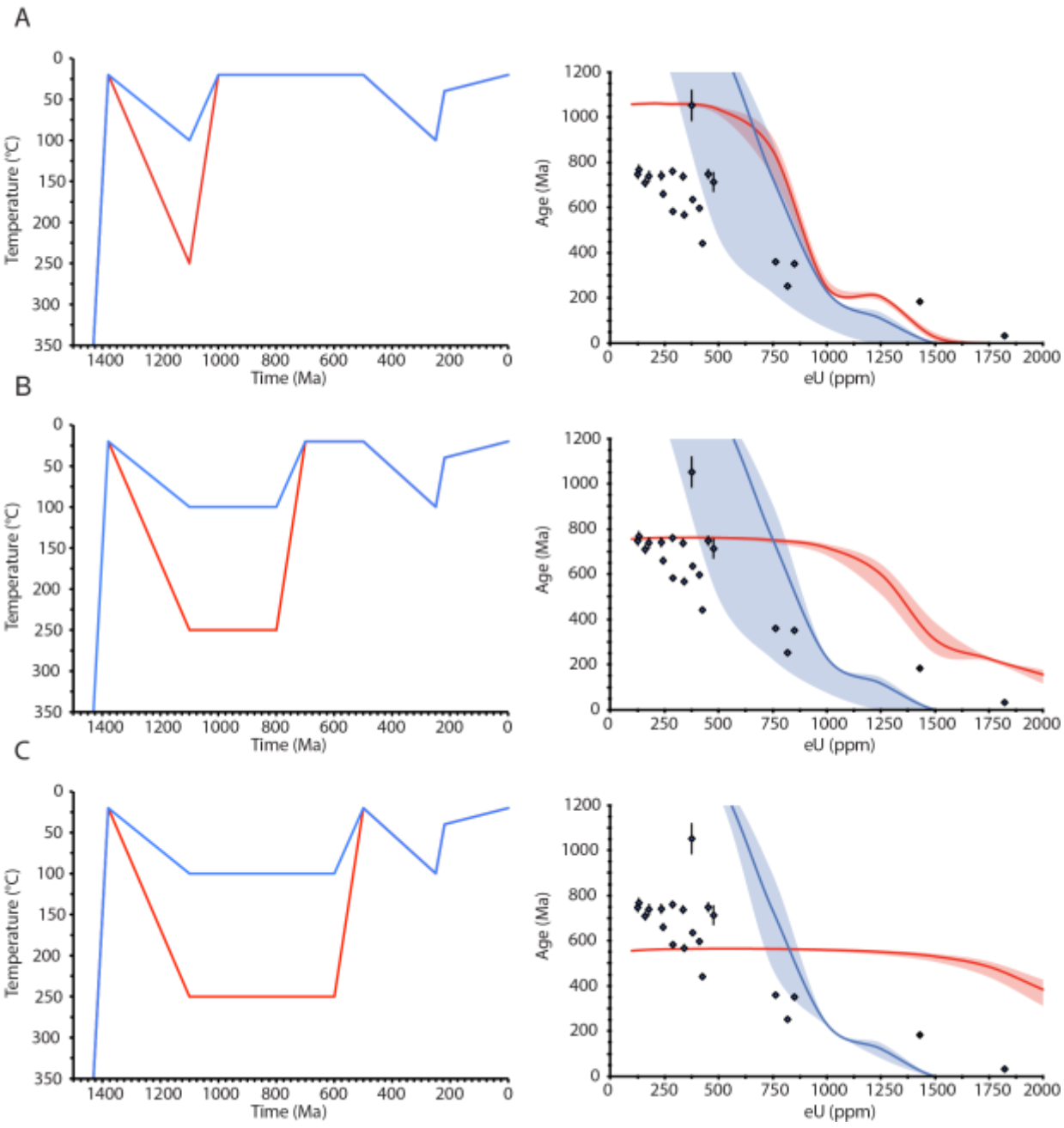

Supplemental Figure DR2: Zircon (U-Th)/He age-eU correlations and forward model results for t-T paths that tested the effects of cooling related to three Proterozoic tectonic episodes: A) Keweenawan rifting at 1100-1000 Ma, B) early Rodinia break-up at 800-700 Ma, and C) Pannotia break-up at 600 and 500 Ma. In all three sub-figures, Proterozoic reheating is set at either 250 or 100 °C, and the results shown here represent brackets for the entire range of forward modeled paths as described in the supplemental text. Left-hand panels show t-T paths while right-hand panels show corresponding age-eU model output (lines and envelopes) and observed data (blue diamonds). Solid curves represent the mean grain size, and slightly transparent envelopes represent the 2-standard deviation grain size.

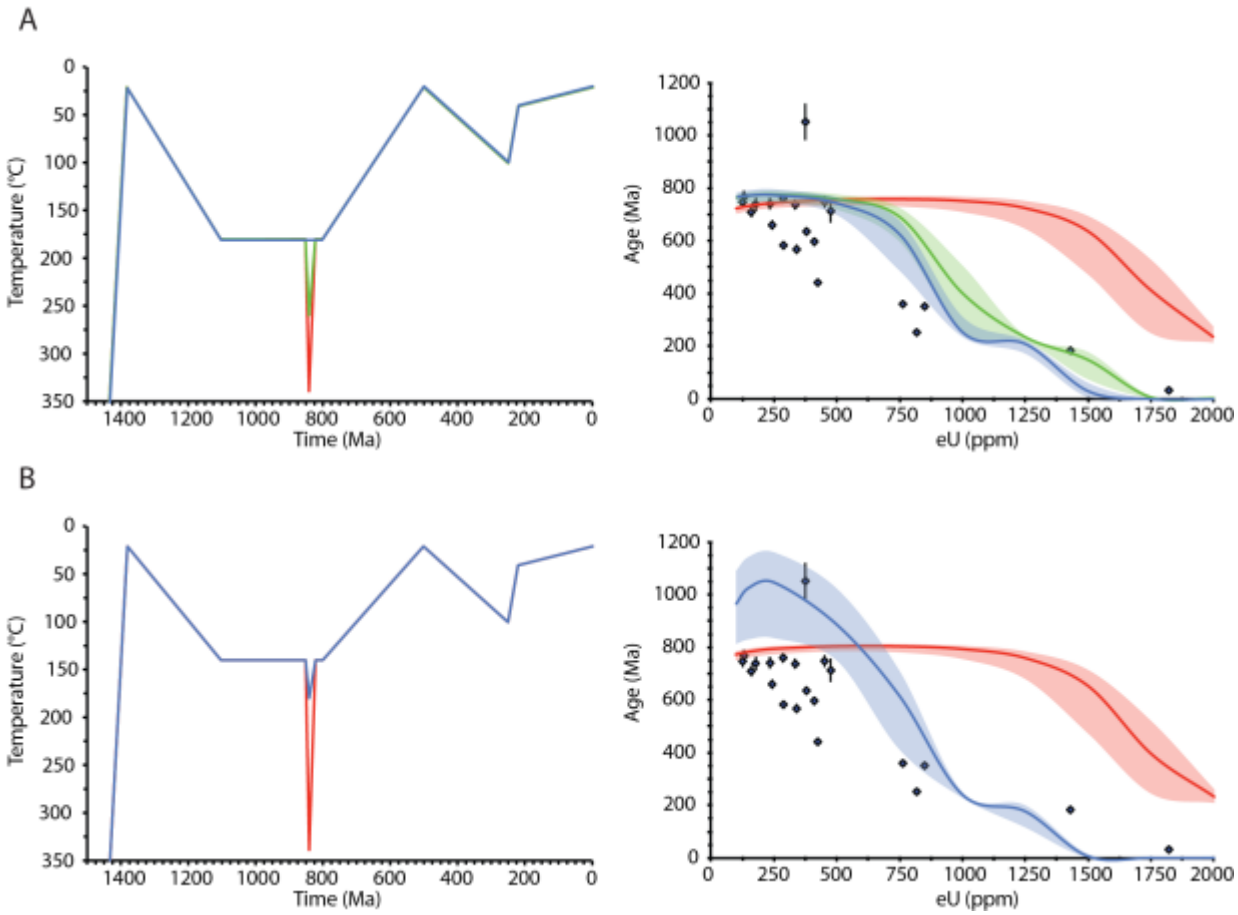

Supplemental Figure DR3: Zircon (U-Th)/He age-eU correlations and forward model results for t-T paths that tested the effects of reheating related to a short-lived, rapid event as a consequence of the initial break-up of Rodinia. Models and figure format were designed to be similar to figure S2, but with a single Neoproterozoic cooling event that combines S2B and S2C for simplicity. A and B vary by the Proterozoic temperatures prior to reheating
(explained in supplementary text). Both models begin reheating at 850 Ma to a maximum temperature at 840 Ma, and cool back to pre-reheating temperatures by 820 Ma. Here we show representative results with no reheating (blue), reheating to 260 °C (green), and reheating to 340 °C (red) in A; and reheating to 180 °C (blue) and 340 ° C (red) in B. Age-eU model outputs indicate that slight reheating does not significantly affect the envelope patterns, but with more reheating, the models lose the plateau-negative correlation-piedmont pattern seen in inverse modeling and observed data.

SUPPLEMENTAL TABLE DR1. ZIRCON (U-Th)/He DATA

Sample Name	Lat.	Long.	Grain size (µg, equiv. sphere rad.)	U (ng)	Analyt. ± (2σ)[1]	U (ppm) Morphology	U (ppm) Isotope Dilution	Th (ng)	Analyt. ± (2σ)[1]	Th (ppm) Morphology	Th (ppm) Isotope Dilution	Zr (ng)	Analyt. ± (2σ)[1]	^{4}He (pmol)	Analyt. ± (2σ)[1]	Ft	Corr. Age (Ma)	Analyt. ± (2σ)[1]
16A075_14OZ01-Z-12	37°39'29	90°41'3	47	1.62	0.05	305	311	3.65	0.110	689	704	2583	87	7.354	0.410	0.74	712.7	44.9
16A076_14OZ01-Z-13			59	2.94	0.09	234	249	6.33	0.199	504	537	5870	184	21.286	1.187	0.79	1051.8	69.3
16A078_14OZ01_Z_15			43	4.02	0.12	1493	1689	1.34	0.041	499	565	1183	36	0.539	0.003	0.72	32.0	0.9
16A079_14OZ01_Z_16			39	0.41	0.01	222	164	1.30	0.039	709	523	1232	37	2.083	0.013	0.69	760.5	18.3
16A081_14OZ08_Z_30	37°36'40	90°37'53	41	1.06	0.03	411	413	0.42	0.013	162	163	1279	39	3.543	0.023	0.72	748.0	22.4
16A082_14OZ08_Z_31			41	0.18	0.01	84	119	0.08	0.003	38	54	739	22	0.609	0.006	0.72	767.5	23.9
16A083_14OZ08_Z_32			36	0.16	0.00	103	110	0.10	0.003	62	66	733	22	0.528	0.005	0.68	746.9	21.8
16A085_14OZ08_Z_33			35	0.20	0.01	150	145	0.08	0.003	61	60	673	21	0.578	0.003	0.67	709.3	21.0
16A086_14OZ08_Z_34			38	0.31	0.01	152	161	0.13	0.005	62	66	948	29	0.987	0.005	0.70	738.9	25.9
16A087_14OZ11_Z_18	37°40'8"	90°23'18"	40	0.52	0.02	242	357	0.33	0.010	155	229	726	22	1.424	0.006	0.71	597.0	16.3
16A088_14OZ11_Z_19			40	2.51	0.08	1195	1246	1.57	0.047	751	783	1001	30	2.006	0.013	0.70	183.1	4.9
16A089_14OZ11_Z_20			41	1.35	0.04	624	714	0.84	0.026	387	443	942	28	1.516	0.010	0.71	252.0	7.3
16A090_14OZ11_Z_21			50	2.85	0.08	687	752	1.58	0.045	381	417	1887	62	4.732	0.029	0.76	350.9	9.2
16A091_14OZ11_Z_22			45	0.78	0.02	272	298	0.41	0.012	145	158	1300	43	2.701	0.018	0.74	737.0	20.1
16A092_14OZ11_Z_23			39	1.02	0.03	570	665	0.64	0.019	359	419	765	26	1.615	0.009	0.69	359.7	9.3
16A093_14OZ11_Z_24	37°48'52"	90°15'3"	64	2.21	0.06	250	261	0.98	0.028	111	116	4220	145	6.4965	0.040	0.81	582.9	15.8
16A094_14OZ12_Z_25			83	8.06	0.23	373	405	1.66	0.048	77	84	9903	402	17.771	0.137	0.85	441.2	12.6
16A095_14OZ12_Z_26			46	1.02	0.03	304	340	0.51	0.015	152	170	1497	50	3.043	0.020	0.75	635.4	17.4
16A096_14OZ12_Z_27			65	1.95	0.06	199	220	0.88	0.025	90	99	4417	145	6.566	0.053	0.82	659.7	19.0
16A097_14OZ12_Z_28			49	1.29	0.04	286	309	0.56	0.016	125	134	2075	68	3.415	0.047	0.76	567.0	17.5
16A098_14OZ12_Z_29			45	0.75	0.02	213	213	0.34	0.010	96	95	1762	59	2.588	0.036	0.74	740.9	23.9

1Formal analytical precision propagated on uncertainties

SUPPLEMENTAL TABLE DR2. APATITE (U-Th)/He DATA

Sample Name	Lat.	Long.	Grain size (µg, equiv. sphere rad.)	U (ng)	Analyt. ± $(2\sigma)^1$	U (ppm) Morphology	U (ppm) Isotope Dilution	Th (ng)	Analyt. ± $(2\sigma)^1$	Th (ppm) Morphology	Th (ppm) Isotope Dilution	Ca (ng)	Analyt. ± $(2\sigma)^1$	^{4}He (pmol)	Analyt. ± $(2\sigma)^1$	Ft	Corr. Age (Ma)	Analyt. ± $(2\sigma)^1$
16A146_14OZ11_A_51	37°40'8"	90°23'18"	44	0.0064	0.00042	4	4	0.023	0.0009	13	15	620	20	0.0084	0.0004	0.68	175.6	10.9
16A147_14OZ11_A_52			37	0.0048	0.00036	5	6	0.012	0.0008	13	15	315	11	0.0049	0.0003	0.63	175.2	12.8
16A148_14OZ11_A_53			38	0.0035	0.00039	4	4	0.011	0.0005	12	13	321	10	0.0037	0.0002	0.64	161.6	13.3
16A149_14OZ11_A_54			57	0.0142	0.00058	4	5	0.047	0.0019	14	15	1207	39	0.0196	0.0009	0.75	175.4	9.7
16A150_14OZ11_A_55			39	0.0088	0.00039	8	5	0.018	0.0009	15	10	699	21	0.0096	0.0005	0.65	198.4	11.7
16A151_14OZ11_A_56			51	0.0115	0.00048	5	6	0.029	0.0013	13	14	810	24	0.0133	0.0007	0.72	179.0	10.8
16A152_14OZ12_A_45	37°48'52"	90°15'3"	63	0.0135	0.00056	4	9	0.040	0.0024	12	25	622	19	0.0179	0.0009	0.77	178.9	10.6
16A153_14OZ12_A_46			74	0.0175	0.00070	3	6	0.041	0.0013	8	13	1263	38	0.0196	0.0010	0.80	153.8	8.6
16A154_14OZ12_A_47			61	0.0213	0.00073	6	13	0.069	0.0024	20	42	663	20	0.0217	0.0010	0.76	134.9	7.2
16A155_14OZ12_A_48			37	0.0095	0.00053	10	8	0.030	0.0016	31	25	465	16	0.0145	0.0007	0.62	246.4	15.3
16A156_14OZ12_A_49			37	0.0092	0.00045	9	10	0.028	0.0009	27	30	368	12	0.0213	0.0010	0.63	376.2	21.6
16A157_14OZ12_A_50			33	0.0102	0.00041	12	8	0.028	0.0009	32	22	508	16	0.0123	0.0006	0.59	219.0	12.2

1Formal analytical precision propagated on uncertainties

Supplemental Table DR3: Fission-Track Data

Sample Number	No. of Crystals	Track Density ($\times 10^6$ tracks.cm^{-2}) (Number of Tracks)			Mean Dpar (μm)	Age Dispersion ($P\chi^2$)	Central Age (Ma) (±1σ)	Apatite Mean Track Length (μm ± 1 s.e.) (no. of tracks)	Standard Deviation (μm)
		ρ_s (N_s)	ρ_i (N_i)	ρ_d (N_d)					
14 02 07	20	0.6920 (314)	1.078 (489)	1.585 (5072)	1.75	<0.01% (97.4%)	**184.6±15.5**	**13.54±0.14 (78)**	**1.23**
14 0Z 11	20	0.3453 (162)	0.4775 (224)	1.570 (5025)	1.81	<0.01% (98.8%)	**205.7±23.0**	**15.66±0.95 (2)**	**0.95**
14 0Z 12	21	0.5902 (377)	0.7938 (507)	1.555 (4978)	1.66	0.13% (98.6%)	**209.4±16.8**	**13.08±0.32 (29)**	**1.70**

Notes:

(i). Analyses by external detector method using 0.5 for the $4\pi/2\pi$ geometry correction factor;

(ii). Ages calculated using dosimeter glass: IRMM540R with ζ_{540R} = 368.1±14.9 (apatite);

(iii). $P\chi^2$ is the probability of obtaining a χ^2 value for v degrees of freedom where v = no. of crystals - 1;

(iv). s.e. = standard error of the mean;